*Journal of Geological Remote Sensing, 2025, 3(1); 56- 70*

Journal of Geological Remote Sensing

Journal homepage: https:// jgrs.kgut.ac.ir

# Surface Scattering Classification Using Dual-Polarization ALOS PALSAR Data in the Zagros Fold–Thrust Belt, SW Iran

Sima Ameri[1*], SeyedAbbas Najafi[2]

[1] MSc Student, Geological Remote Sensing, Department of Remote Sensing & GIS, Faculty of Geology, Shahid Chamran University of Ahwaz, Ahwaz, Iran., [2] MSc. Student, Petroleum Engineering - Exploration, Department of Petroleum Engineering, Abadan Faculty of Petroleum, Petroleum University of Technology, Abadan, Iran.

Article Info

**Keywords:**
SAR Surface Roughness, Dual-Polarization SAR, Unsupervised Clustering, ALOS PALSAR, Zagros Fold–Thrust Belt.

Abstract

This study presents a framework for identifying terrain-related surface scattering regimes using dual-polarization ALOS PALSAR (L-band) data over a 4,852 km² area in the central Zagros Fold–Thrust Belt, SW Iran. The methodology integrates three complementary radar-derived features: (1) a surface roughness proxy computed from spatial gradients of HH backscatter intensity, (2) the Polarization Ratio (PR), and (3) a modified Radar Vegetation Index (RVI). Following radiometric preprocessing and speckle reduction, features were log-transformed, standardized, and reduced using Principal Component Analysis (PCA). K-means clustering as a unsupervised classification was applied to the standardized SAR-derived features in order to identify five dominant scattering classes across the study area. Class-wise roughness distributions exhibit marked contrasts, ranging from highly homogeneous and low-roughness conditions to strongly heterogeneous and high-roughness domains. One-way ANOVA results indicate very strong statistical separation among classes ($p < 0.001$, $\eta^2 = 0.801$), signifying that over 80% of the total roughness variance is explained by class membership. High-roughness classes account for approximately 26.6% of the mapped area, and global roughness percentiles reveal a pronounced right-tailed distribution consistent with heterogeneous structural conditions. These results demonstrate that intensity-based roughness metrics combined with dual-polarization SAR indicators effectively capture spatial variability in radar scattering behavior. The framework is computationally efficient and objective, suitable for large regions. Although the resulting classes represent statistical scattering regimes rather than explicit geomorphological categories, the strong internal separability and spatial coherence of the clusters highlight the capability of L-band SAR to capture regional-scale surface heterogeneity. This approach offers a practical framework for unsupervised terrain analysis in structurally complex environments.

Corresponding author. Sima Ameri
*Email:* sa.geolove2@gmail.com

https://doi.org/10.48306/jgrs.2026.530660.1014
Received August 2025; Accepted October 2025

## 1. Introduction

Automated extraction of terrain-related information from satellite data plays a critical role in geomorphological and structural analysis, particularly in tectonically active or inaccessible regions. Synthetic Aperture Radar (SAR) systems provide a significant advantage in this context because they operate independently of daylight and weather conditions and are sensitive to surface structure and dielectric properties (Bamler & Hartl, 1998; Moreira et al., 2013). In particular, L-band SAR, with its longer wavelength, exhibits enhanced sensitivity to surface roughness and structural heterogeneity at intermediate spatial scales. Dual-polarization SAR data offer additional insights into scattering behavior through the combination of co-polarized and cross-polarized returns. Polarimetric indicators derived from HH and HV channels, such as polarization ratios and vegetation-related indices, have been widely used to characterize surface structure and scattering complexity (Cloude, 2010; Shimada et al., 2010; Touzi & Bhattacharya, 2011; Lee & Pottier, 2017). However, many existing classification approaches rely either on ancillary topographic datasets (e.g., DEM-derived slope and curvature) or on supervised machine learning methods requiring extensive training data. In data-limited environments, such requirements may restrict operational applicability.

The Zagros Fold–Thrust Belt in southwestern Iran represents a structurally complex and tectonically active region shaped by the ongoing convergence between the Arabian and Eurasian plates (Alavi, 1994; Berberian, 1995; Abdollahie Fard et al, 2006). Within this belt, the transition between the Dezful Embayment and the Izeh Zone is characterized by contrasting structural styles, lithological variability, and pronounced differences in surface morphology. These characteristics generate spatial variability in radar backscatter behavior, making the region an appropriate test site for SAR-based terrain classification.

This study presents a framework for identifying terrain-related surface scattering regimes using single-date dual-polarization ALOS PALSAR data. The methodology integrates three key components: (1) a radar-derived roughness proxy based on spatial gradients of HH backscatter; (2) polarimetric indicators, including the Polarization Ratio (PR) and a modified Radar Vegetation Index (RVI); and (3) a workflow utilizing Principal Component Analysis (PCA) for feature space exploration and unsupervised K-means clustering for unit delineation. The objective is to delineate statistically distinct surface scattering regimes rather than labeling predefined landform categories. The central research question is whether intensity-based roughness and dual-polarization indicators alone can capture the major spatial contrasts associated with the structural transition between the Dezful Embayment and the Izeh Zone. By evaluating the statistical separability and spatial distribution of the resulting classes across a 4,852 km² area, this study assesses the capability of a transparent, computationally efficient SAR-based framework to characterize regional-scale surface heterogeneity without reliance on external topographic data.

## 2. Study area

The study area is situated between Khuzestan and Kohgiluyeh & Boyer-Ahmad provinces in southwestern Iran (Figure 1). This region includes the counties of Ramhormoz, Baghmalek and Omidiyeh in Khuzestan Province, as well as Bahmai and Kohgiluyeh in Kohgiluyeh & Boyer-Ahmad Province, with an average elevation of 659 meters above sea level. The study area spans latitudes 30° 55' to 31° 31' N and longitudes 49° 30' to 50° 16' E, covering an approximate area of 4,852 km². In addition to its geographic setting, the study area lies within the central part of the Zagros Fold–Thrust Belt, which forms part of the Alpine–Himalayan orogenic system and resulted from the ongoing convergence between the Arabian and Eurasian plates (Falcon, 1961; Alavi, 1994). Structurally, the region encompasses portions of the Dezful Embayment and the Izeh Zone, two major tectono-sedimentary domains of the Zagros basin (Berberian, 1995; Alavi, 2004). The Dezful Embayment is characterized by thick Cenozoic sedimentary successions and relatively gentle folding compared with adjacent structural zones, whereas the Izeh Zone exhibits more intense deformation and complex structural patterns. The tectonic architecture of the region is controlled by several major structural elements, including NW–SE trending anticlines and synclines typical of the Zagros Simply Folded Belt, as well as deep-seated fault systems such as the Mountain Front Fault (MFF) and the Kazerun fault system (Berberian & King, 1981; Hessami et al., 2001). These structures reflect the compressional regime generated by the Arabia–Eurasia collision, which continues today with a convergence rate of approximately 20–25 mm/yr (Sella et al., 2002). The structural framework also includes several basements-controlled fault trends with N–S, NW–SE, and NE–SW orientations that influence fold development and regional deformation patterns (Alavi, 2004).

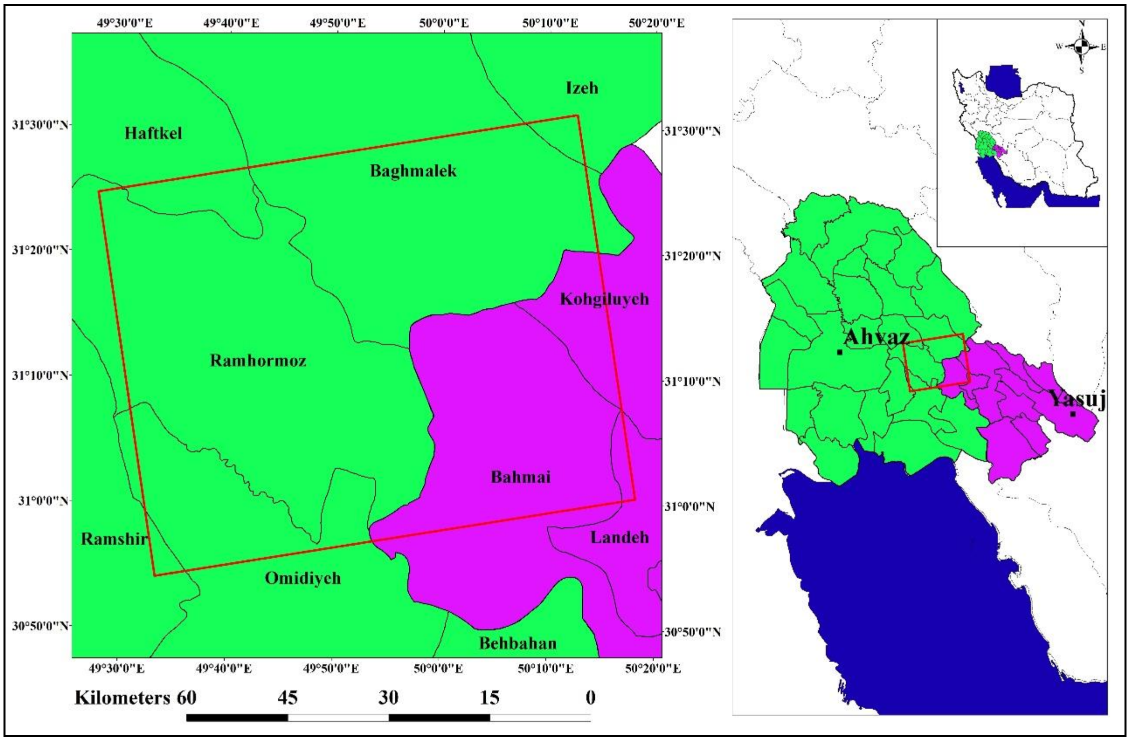

**Figure 1.** Location of the study area between Khuzestan and Kohgiluyeh & Boyer-Ahmad provinces.

Stratigraphically, the exposed formations within the study area mainly belong to the Neogene succession of the Zagros basin and include the Gachsaran, Mishan, Aghajari, and Bakhtiari formations (Motiei, 1993; Sherkati & Letouzey, 2004). These units consist predominantly of evaporites, marls, sandstones, conglomerates, and carbonate rocks. The mechanical contrast between these lithological units—particularly the ductile evaporites of the Gachsaran Formation and the more competent clastic units of the Aghajari and Bakhtiari formations—plays a key role in controlling folding style, surface morphology, and slope development (Sherkati et al., 2005).

Consequently, the present-day topography of the region largely reflects its structural and lithological framework. Folded ridges, structural valleys, and fault-controlled escarpments generate significant spatial variations in surface roughness and slope geometry, which strongly influence radar backscatter patterns in SAR imagery. These geological and geomorphological characteristics therefore provide an important physical basis for the SAR-based topographic classification approach employed in this study (Berberian, 1995; Alavi, 2004).

Figure 2 presents a simplified geological map of the study area showing the distribution of major formations and structural elements including anticlines, synclines, and major fault systems.

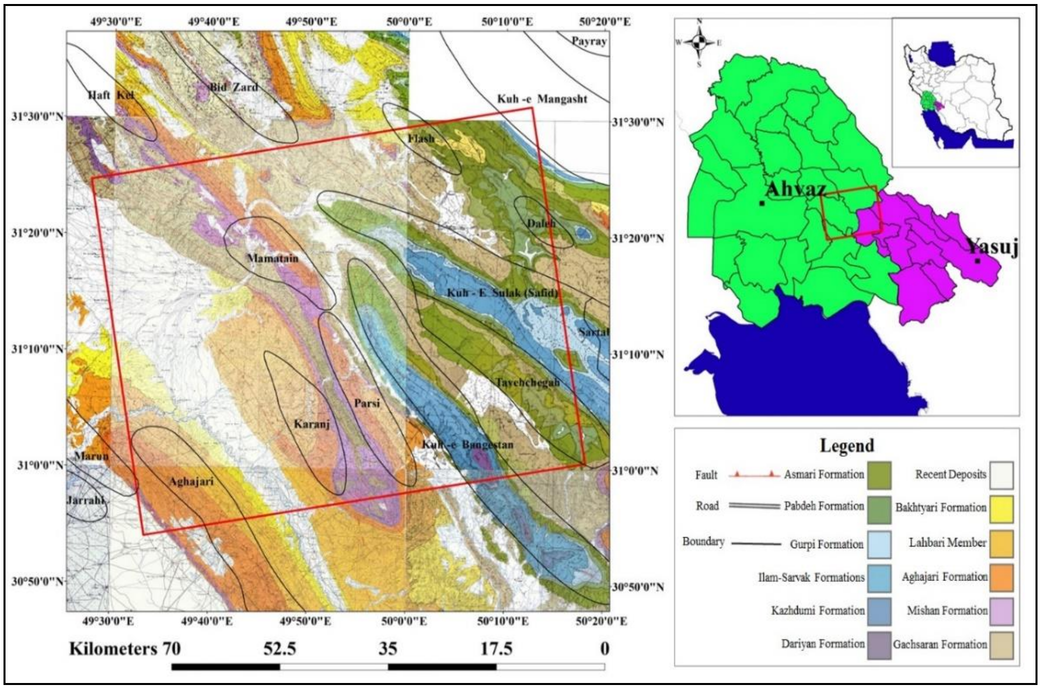

**Figure 2.** Geological map of the study area.

## 3. Materials and Methods

This study utilized L-band Synthetic Aperture Radar (SAR) data acquired by the ALOS PALSAR Level 2.2 on 18 September 2007. The dataset includes dual-polarization channels (HH and HV) with a spatial resolution of 12.5 m, which are suitable for characterizing variations in radar backscatter associated with surface roughness and scattering mechanisms.

L-band SAR is particularly advantageous for terrain analysis because its longer wavelength allows deeper penetration through sparse vegetation and increased sensitivity to surface roughness and structural characteristics of the ground surface. The SAR data were orthorectified using the AW3D30 digital elevation model with the EGM96 geoid model to ensure geometric consistency and accurate spatial alignment.

Several radar-derived indicators, including HH and HV backscatter, the polarization ratio (PR), the modified radar vegetation index (RVI), and a surface-roughness proxy, were generated from the SAR observations to represent different surface scattering characteristics. These variables collectively describe surface scattering, volumetric scattering, and spatial heterogeneity in the radar response. The overall methodological workflow, as illustrated in Figure 3, encompasses SAR preprocessing, feature extraction, feature integration and exploratory analysis, and unsupervised classification followed by visualization.

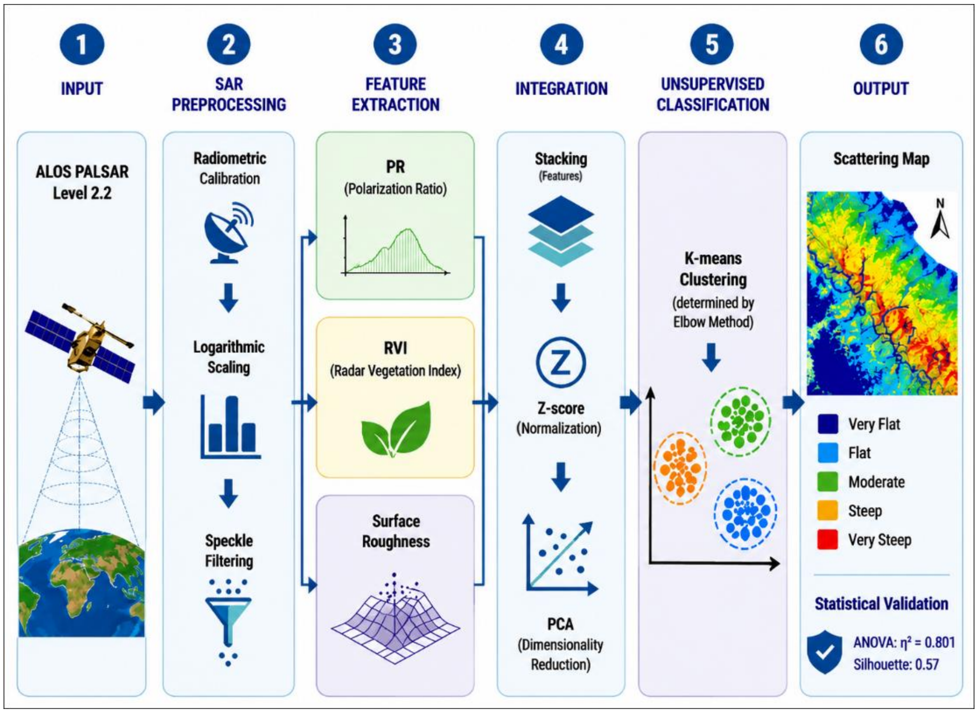

**Figure 3.** Methodological workflow for processing ALOS PALSAR data. The procedure follows a sequential approach starting from data input (Step 1), SAR preprocessing (Step 2), and feature extraction (Step 3) to feature integration and exploratory analysis (Step 4). Finally, the workflow concludes with unsupervised K-means classification (Step 5) and the generation of a scattering map with statistical validation metrics (Step 6).

### 3.1. SAR Preprocessing

Radiometric preprocessing was applied to prepare the calibrated backscatter data for analysis. Amplitude values were converted to intensity according to:

$$I = |A|^2$$

Where:

A represents the radar amplitude and I denotes the radar intensity.

The intensity values were then converted to the sigma-naught backscatter coefficient ($\sigma^0$) using logarithmic scaling:

$$\sigma^0(dB) = 10\ \log_{10}(I)$$

Where:

$\sigma^0$ represents the normalized radar backscatter coefficient expressed in decibels (dB).

The dataset provides calibrated $\sigma^0$ backscatter values. Intensity conversion and logarithmic scaling were applied for analysis.

To reduce speckle noise while preserving spatial structures, a 3×3 median filter was applied to the calibrated backscatter images.

## 3.2. Feature Extraction

### 3.2.1. Polarimetric Feature Extraction

Two polarimetric indicators including; Polarization Ratio (PR) and Radar Vegetation Index (RVI) were derived from the dual-polarization SAR data to capture variations in radar scattering mechanisms.

The polarization ratio highlights differences between co-polarized and cross-polarized backscatter and is defined as:

$$PR = \frac{HV}{HH}$$

This ratio highlights relative differences between cross-polarized and co-polarized returns and is sensitive to changes in surface structure and scattering complexity.

A modified Radar Vegetation Index (RVI) was calculated as:

$$RVI = \frac{4HV}{HH + HV}$$

RVI is widely used as an indicator of volume scattering, typically associated with vegetation or structurally complex surfaces. In this study, RVI is not interpreted as a direct indicator of terrain slope; instead, it serves as a proxy for scattering complexity, helping differentiate areas dominated by volume scattering from those characterized by surface scattering.

These parameters are widely used in SAR polarimetric analysis to characterize surface and volume scattering mechanisms (Lee & Pottier, 2017). To reduce skewness and stabilize variance, a logarithmic transformation ($\log_{10}$) was applied to PR. For RVI, a small constant ($\varepsilon = 0.01$) was added prior to transformation, resulting in $\log_{10}(RVI + \varepsilon)$, to avoid large negative values near zero and ensure numerical stability.

### 3.2.2. Radar-Derived Surface Roughness Proxy

A radar-based proxy for surface roughness was derived from spatial variations in the HH backscatter channel. The HH polarization was used for roughness estimation because co-polarized backscatter in L-band SAR is generally more sensitive to surface roughness and dielectric contrasts than cross-polarized returns. The roughness indicator was computed using the gradient magnitude of the HH backscatter image, which measures local spatial variability in radar response:

$$R = \sqrt{(\frac{\partial HH}{\partial x})^2 + (\frac{\partial HH}{\partial y})^2}$$

Where:

R represents the roughness proxy derived from spatial gradients of the HH backscatter.

To suppress high-frequency noise, the gradient image was smoothed using a Gaussian filter. Extreme values were removed through percentile clipping (1–99%), and the resulting roughness values were normalized to a range of 0–1 to facilitate integration with other features. This parameter does not represent geometric slope but rather reflects spatial variability in radar backscatter associated with surface roughness and structural heterogeneity.

### 3.3. Feature Integration and Exploratory Analysis

Three complementary feature layers were integrated to form a multidimensional feature space:

- Radar-derived roughness proxy
- Log-transformed polarization ratio
- Log-transformed radar vegetation index

Prior to analysis, all variables were standardized using z-score normalization:

$$z = \frac{x - \mu}{\sigma}$$

Where:

x represents the feature value, μ is the mean, and σ is the standard deviation. This normalization ensures that all variables contribute equally to the subsequent analysis.

Principal Component Analysis (PCA) was applied to the normalized dataset to reduce redundancy and capture the dominant patterns within the feature space. In the present study, PCA was used solely for exploratory analysis and visualization, rather than for clustering. The first two principal components explained 93.71% of the total variance, indicating that the majority of information contained within the feature space is preserved in a two-dimensional representation.

### 3.4. Unsupervised Classification and Visualization

Surface scattering classes were identified using the K-means clustering algorithm, an unsupervised machine learning method that partitions data into clusters based on similarity in feature space.

K-means iteratively assigns each pixel to the nearest cluster centroid while minimizing the within-cluster variance:

$$J = \sum_{i=1}^{k} \sum_{x_j \in C_i} \left\| x_j - \mu_i \right\|^2$$

Where:

$C_i$ represents cluster i, $\mu_i$ is the centroid of cluster i, and $x_j$ denotes individual observations.

The number of clusters was set to five (k = 5) to capture the primary variations in SAR scattering behavior across the study area while maintaining interpretable class separation. This configuration provided a balanced representation of dominant surface scattering regimes without excessive fragmentation of classes. The optimal number of clusters was determined through preliminary clustering experiments using the elbow method, which evaluates the reduction in within-cluster sum of squares (WCSS) as a function of k. The elbow analysis was conducted for k values ranging from 2 to

10. The resulting curve exhibited a clear inflection point at k = 5, indicating diminishing returns in variance reduction beyond this value. This selection provides a balance between cluster compactness and interpretability while avoiding over-fragmentation of scattering regimes. All derived indicators, including radar-based roughness, polarization ratio, and RVI, as well as the final five-class terrain classification, were visualized using thematic maps to facilitate interpretation of spatial variability in radar scattering responses. These visualizations facilitate interpretation of spatial variability in radar scattering responses and support qualitative assessment of terrain complexity.

### 3.4.1. Statistical Validation of Classification

To statistically validate the distinctiveness of the five generated scattering classes, a one-way Analysis of Variance (ANOVA) was performed on the radar-derived surface roughness proxy values. This analysis aimed to determine if significant differences exist in the mean roughness among the classified clusters. The ANOVA was conducted using MATLAB. A significance level of $p < 0.05$ was adopted for all statistical tests. Furthermore, to provide a more robust measure of class separation strength, especially given the large sample size, the effect size was quantified using Eta squared ($\eta^2$). Cluster separability was also evaluated using the silhouette coefficient, computed from a random sample of 10,000 pixels, to assess the compactness and separation of the clusters in the feature space.

## 4. Results

### 4.1. Spatial Distribution of Surface Scattering Classes

The unsupervised classification identified five dominant surface scattering classes, each representing a characteristic combination of backscatter roughness and polarimetric behavior. These classes exhibit a heterogeneous spatial pattern across the study area, reflecting substantial variations in local scattering conditions. The resulting spatial configuration of the clusters is depicted in the K-means-derived classification map presented in Figure 4.”

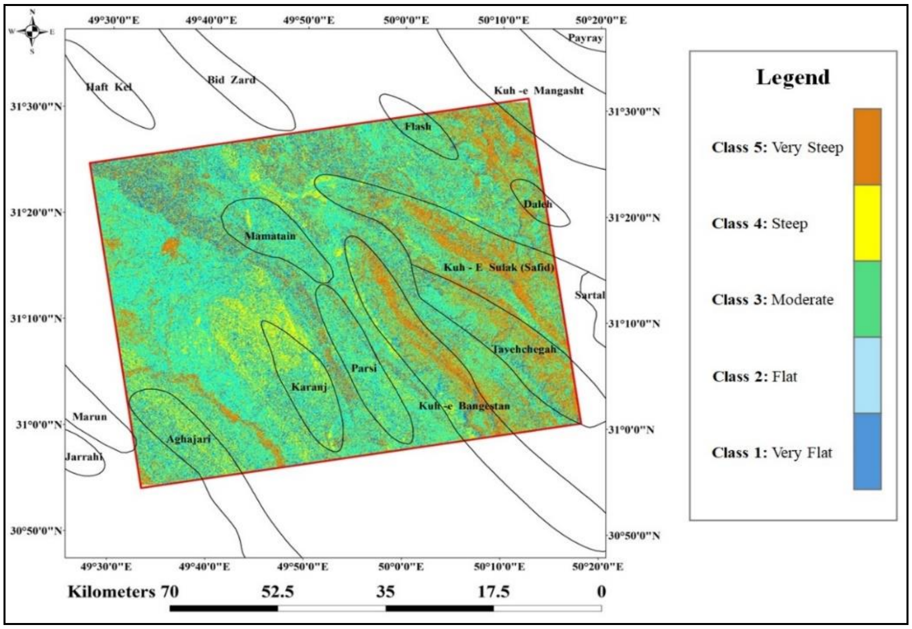

**Figure 4.** Spatial distribution of the five surface scattering classes derived from K-means clustering.

The total extent of the analyzed area is approximately 4,852 km², with class-wise area distribution summarized in Table 1. Class 1 forms the largest mapped unit (25.33% of total area), while Class 4 represents the smallest but most distinctive high-roughness domain (12.01%). Combined, the upper roughness classes (Classes 4 and 5) cover 26.60% of the region, highlighting the presence of zones with markedly elevated textural variability. The relatively balanced distribution of classes suggests that the clustering algorithm effectively captured multiple dominant scattering regimes rather than producing highly skewed class proportions.

**Table 1.** Area and pixel distribution for the five surface scattering classes.

| Class | Pixel Count | Area (km²) | Percent of Area |
|---|---|---|---|
| 1 | 7,866,593 | 1229.16 | 25.33% |
| 2 | 6,412,458 | 1001.95 | 20.65% |
| 3 | 7,570,559 | 1182.90 | 24.38% |
| 4 | 3,730,751 | 582.93 | 12.01% |
| 5 | 5,474,968 | 855.46 | 17.63% |

## 4.2. Descriptive Statistics of Roughness Distributions

To visualize the spatial variability of radar-derived surface roughness, the normalized roughness proxy map is presented in Figure 5.

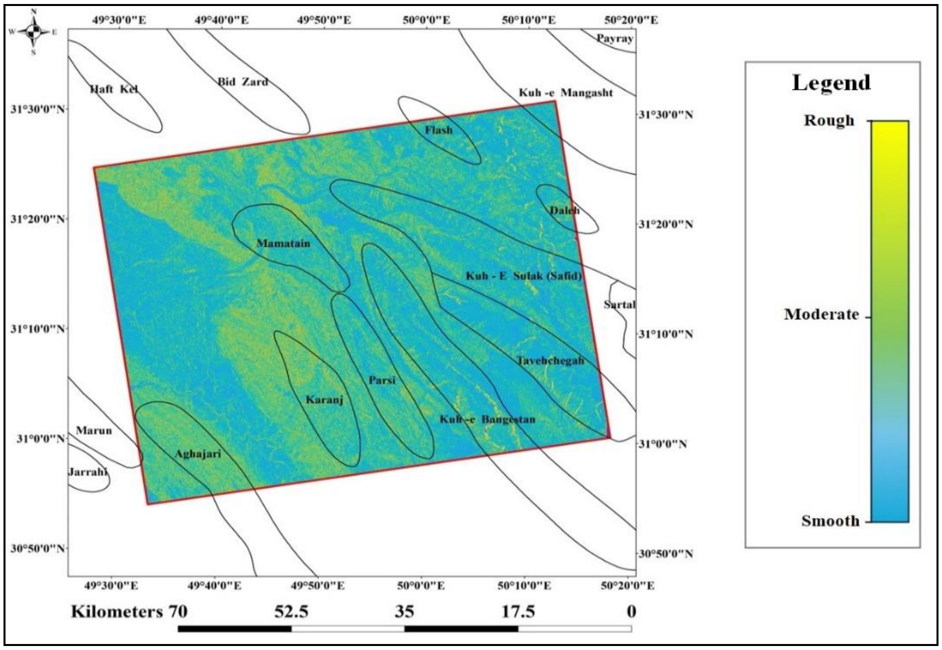

**Figure 5.** Spatial distribution of the normalized SAR-derived roughness proxy calculated from the gradient of the median-filtered HH backscatter.

Significant variability in surface roughness was observed across the classes (Table 2).

Class 1 shows extremely low roughness values with a strongly right-tailed distribution (skewness = 24.31). This behavior results from the large proportion of pixels with near-zero gradient values in homogeneous backscatter regions, combined with a small number of higher roughness values that produce a long positive tail, which is fully consistent with a highly homogeneous scattering regime.

Classes 2 and 3 represent mid-range roughness with moderate dispersion, while Class 4 contains the highest roughness values and the widest dynamic range.

Class 5 exhibits intermediate-to-high roughness with the highest relative dispersion among the mid-range classes (CV = 0.2975).

Global roughness percentiles are as follows:

- P10 = 0.000
- P25 = 0.2715
- P50 = 0.4370
- P75 = 0.5745
- P90 = 0.7141

These values indicate that the majority of surface elements fall within a moderate roughness interval, with a long tail toward highly heterogeneous scattering zones.

**Table 2.** Descriptive statistics of normalized roughness for all classes.

| Class | Mean | Std | Median | Min | Max | Skewness | Kurtosis | CV | Mean Z-Score |
|---|---|---|---|---|---|---|---|---|---|
| 1 | 0.0010 | 0.0213 | 0.0000 | 0.0000 | 0.6104 | 24.31 | 615.35 | 22.255 | -1.4608 |
| 2 | 0.4731 | 0.1249 | 0.4643 | 0.0980 | 1.0000 | 0.8699 | 5.2559 | 0.2641 | 0.4272 |
| 3 | 0.4228 | 0.0940 | 0.4219 | 0.0864 | 0.7266 | 0.0334 | 2.5169 | 0.2223 | 0.2261 |
| 4 | 0.6643 | 0.1655 | 0.6616 | 0.0743 | 1.0000 | 0.0359 | 2.4459 | 0.2491 | 1.1920 |
| 5 | 0.4847 | 0.1442 | 0.4654 | 0.1003 | 1.0000 | 0.7945 | 3.8486 | 0.2975 | 0.4736 |

### 4.3. Statistical Significance of Class Separation

To examine whether the five classes represent statistically distinct surface scattering regimes, a one-way ANOVA was conducted on the roughness values.

The ANOVA results indicate extremely strong statistical separation among the classes:

- $F(4, 31{,}055{,}324) = 3.12 \times 10^7$
- $p < 0.001$

The extremely large F-value is partly influenced by the very large sample size typical of pixel-based remote sensing datasets, where even small differences can yield very high statistical significance.

Given the large sample size, the effect size provides a more meaningful indicator of separation strength:

- Eta squared ($\eta^2$) = 0.801

This shows that 80.1% of the total variance in roughness is attributable to differences between the five classes—a very large effect size that confirms the robustness of the clustering outcome.

**Table 3.** One-way ANOVA summary for roughness across classes.

| Source | SS | df | MS | F | p-value |
|---|---|---|---|---|---|
| Between Groups | 1,555,413.6 | 4 | 388,853.4 | $3.124\times10^7$ | $< 0.001$ |
| Within Groups | 386,532.8 | 31,055,324 | 0.000012 | – | – |
| Total | 1,941,946.4 | 31,055,328 | – | – | – |

Cluster separability was further evaluated using the silhouette coefficient computed from a random sample of 10,000 pixels, yielding an average score of 0.57. This value indicates moderate to strong separation between clusters and supports the robustness of the five-class partitioning in feature space.

### 4.4. Overall Roughness Variability and Quantitative Summary

The global coefficient of variation (CV = 65.10%) highlights strong heterogeneity in surface texture at the regional scale. This variability is consistent with the presence of multiple scattering environments captured by the SAR-derived indices and reinforces the relevance of the classification structure. The unsupervised classification identified five statistically distinct surface-scattering classes, with roughness distributions differing markedly in both magnitude and shape. The classification structure explains a substantial portion of roughness variability ($\eta^2 = 0.801$), while high-roughness classes account for 26.6% of the mapped area. Additionally, the roughness percentiles display a long right-skewed tail, reflecting heterogeneous terrain-scattering conditions. Collectively, these findings demonstrate that SAR-derived roughness and polarimetric features provide a strong and consistent quantitative basis for delineating surface-scattering regimes.”

## 5. Discussion

### 5.1. Interpretation of Surface Scattering Classes

The five surface-scattering classes identified in this study represent statistically distinct regimes of radar response that emerge from a combination of L-band backscatter intensity, polarimetric indicators, and a gradient-based roughness metric. Because the methodology relies exclusively on image-derived properties, the resulting classes should be interpreted as scattering units rather than geomorphological landforms or land-cover categories.

Class 1 exhibits the lowest roughness values and an extremely skewed distribution, characterized by frequent near-zero gradients and occasional isolated high values. This pattern is typical of spatially homogeneous radar-return regions, where local variations in HH intensity are minimal. In such conditions, the applied roughness proxy amplifies small differences and produces a strongly right-tailed distribution. Similar behavior is commonly observed in SAR-based texture analyses of homogeneous surfaces, particularly in uniform surfaces where speckle-reduced intensity remains stable over short spatial windows.

Classes 2 and 3 occupy intermediate portions of the roughness spectrum and show moderate variability, reflecting surfaces where backscatter fluctuations are more pronounced than in Class 1 but still not dominated by strong structural heterogeneity. Their distributional properties, including modest skewness and balanced interquartile ranges, suggest environments with a mixture of micro-scale smoothness and localized variations in surface scattering behavior.

Class 4 corresponds to the highest roughness levels, indicating surfaces with substantial local gradients and marked spatial heterogeneity. These surfaces generate more abrupt changes in HH intensity, possibly due to variations in surface structure, dielectrics, or microtopographic conditions that enhance local scattering contrasts. Class 5, although not as extreme as Class 4 in mean roughness, shows the largest relative dispersion (CV = 0.2975), suggesting that it captures scattering environments where roughness is both elevated and highly variable within the class.

The overall separation among classes demonstrates that L-band scattering information, particularly when augmented with a roughness proxy, can delineate meaningful structural variability even in complex terrains. These interpretations are consistent with established SAR physics principles, where backscatter variability is influenced by surface structure, moisture contrasts, and small-scale geometric irregularities.

### 5.2. Statistical Robustness of the Classification

The statistical analysis reveals that the proposed feature set—consisting of HH intensity, polarimetric ratios, and a radar-derived roughness metric—successfully captures the major modes of variability within the dataset. The very high effect size obtained from the one-way ANOVA ($\eta^2 = 0.801$) indicates that class membership explains over 80% of the total variation in the roughness variable. Such a large effect size indicates strong internal coherence of the clustering outcome. The class-wise distributional contrasts further reinforce the discriminative power of the approach. Roughness percentiles show non-overlapping behavior across the five classes, with each class occupying a distinct range of the roughness spectrum. The strong positive skewness and large kurtosis observed in Class 1, while initially appearing extreme, align with the expected statistical signature of a gradient-derived metric applied to homogeneous scattering regions. This provides additional evidence that the classification accurately reflects underlying structural variability rather than noise.

The PCA-based dimensionality reduction step offers further support for the stability of the classification. The separation of classes within the reduced feature space indicates that the combined metrics effectively capture independent patterns of scattering variability. This agreement between clustering and dimensionality reduction demonstrates that the class boundaries do not arise from an artifact of K-means initialization but from genuinely distinguishable scattering signatures.

Collectively, these findings highlight that the methodology is both statistically sound and sensitive to meaningful surface variability, making it a promising framework for terrain analysis in SAR applications.

### 5.3. Advantages of the SAR Approach

A major strength of this study is its reliance on a methodology that does not require a Digital Elevation Model (DEM). By depending exclusively on radar-derived metrics, especially intensity-based roughness and polarimetric ratios, the approach remains robust in regions where high-resolution, high-quality DEM data are limited, unavailable, or inconsistent. This characteristic enhances the applicability of the method to vast geographic areas, including remote, mountainous, or data-sparse regions.

The use of L-band SAR offers additional advantages due to its deep penetration capability and sensitivity to structural features. Unlike shorter wavelengths, L-band is less affected by fine-scale surface irregularities and is more responsive to broader structural patterns, making it particularly suitable for roughness characterization and terrain-related scattering analysis. Furthermore, because the method does not depend on prior land-cover information or ancillary datasets, it avoids potential biases associated with multi-source data integration. The unsupervised nature of the approach ensures that scattering classes emerge solely from the inherent properties of the radar signal, providing an objective delineation of local surface variability. Together, these characteristics position the method as a practical tool for large-area surface characterization, especially where ancillary data are unavailable or unreliable.

### 5.4. Limitations and Future Research Directions

While the results are promising, several limitations should be acknowledged. First, the classification strictly represents statistical scattering units rather than explicit physical or geomorphological categories. Without supplementary datasets such as multispectral imagery, high-resolution DEMs, or field observations, the physical interpretation of each class remains limited to SAR-derived properties. Second, the roughness metric employed in this study is based on spatial derivatives of HH intensity and does not incorporate phase-based information such as interferometric coherence or polarimetric decompositions. Although intensity gradients capture meaningful aspects of structural variability, phase-related metrics could substantially enrich the characterization of surface roughness and enhance class separability. Third, the study utilizes a single-date SAR acquisition. Multitemporal or seasonal datasets would provide insights into the stability of scattering regimes and their sensitivity to moisture, vegetation phenology, or surface disturbance. Incorporating temporal variability into the clustering framework could yield more robust and persistent surface-scattering units. Overall, the findings of this study highlight the potential of radar-derived indicators for unsupervised terrain analysis and surface characterization, demonstrating that a SAR-based approach can capture meaningful structural variability in complex landscapes.

Future research may therefore explore several directions:

- integrating multi-frequency or full-polarimetric SAR datasets to capture a broader range of scattering mechanisms
- comparing the derived classes with terrain attributes from high-resolution DEMs, where available, to examine potential relationships with physical geomorphology
- applying multitemporal SAR stacks to assess temporal stability and derive dynamic scattering regimes
- combining SAR-derived roughness metrics with optical texture and structural indicators to improve interpretability

## 6. Conclusion

This study demonstrates that dual-polarization ALOS PALSAR data, combined with image-derived roughness and polarimetric indicators, provide a robust basis for identifying terrain-related surface scattering regimes without relying on external topographic datasets. By integrating radar-based roughness, polarization ratio, and a modified RVI into a standardized multi-feature space, followed by PCA and K-means clustering, five statistically distinct surface scattering classes were delineated across the 4,852 km² study area. The results show strong variability in surface roughness distributions, ranging from highly homogeneous scattering conditions in Class 1 to strongly heterogeneous, high-roughness domains in Classes 4 and 5. Statistical analysis confirms that class membership accounts for more than 80% of the total roughness variance ($\eta^2 = 0.801$), indicating that the classification captures meaningful structural differences rather than random or noise-driven variability. The global roughness percentiles and coefficient of variation further highlight substantial spatial heterogeneity across the region.

The methodological framework offers three main advantages:

1. It does not rely on external topographic data and is therefore suitable for regions lacking reliable elevation information;
2. It leverages the structural sensitivity of L-band SAR to characterize surface variability at the radar wavelength scale;
3. It provides an objective, data-driven delineation of scattering environments without requiring prior land-cover or ancillary information.

Despite these strengths, the approach is limited by its reliance on intensity-based metrics and single-date observations. Future research may build on this work by incorporating multi-frequency or fully polarimetric SAR, multitemporal datasets, and comparisons with independent terrain or optical texture metrics to improve physical interpretability of the classes. Overall, the findings demonstrate that SAR-derived indicators can effectively characterize large-scale variability in surface scattering behavior and offer a practical foundation for unsupervised terrain analysis in complex or data-limited environments.

## References

1. Abdollahie Fard, I., Braathen, A., Mokhtari, M., & Alavi, S. A. (2006). Interaction of the Zagros Fold-Thrust Belt and the Arabian-type, deep-seated folds in the Abadan Plain and the Dezful Embayment, SW Iran. Petroleum Geoscience, 12(4), 347-362. (DOI: 10.1144/1354-079305-706)
2. Alavi, M. (1994). Tectonics of the Zagros orogenic belt of Iran: new data and interpretations. Tectonophysics, 229(3-4), 211-238. (DOI: 10.1016/0040-1951(94)90030-2)
3. Alavi, M. (2004). Regional stratigraphy of the Zagros fold-thrust belt of Iran and its proforeland evolution. American Journal of Science, 304(1), 1-20. (DOI: 10.2475/ajs.304.1.1)
4. Bamler, R., & Hartl, P. (1998). Synthetic aperture radar interferometry. Inverse Problems, 14(4). (DOI: 10.1088/0266-5611/14/4/001)
5. Berberian, M. (1995). Master “blind” thrust faults hidden under the Zagros folds: active basement tectonics and surface morphotectonics. Tectonophysics, 241(3-4), 193-224. (DOI: 10.1016/0040-1951(94)00185-C)
6. Berberian, M., & King, G. (1981). Toward a Paleogeography and Tectonic Evolution of Iran. Canadian Journal of Earth Sciences, 18, 210-265. (DOI: 10.1139/e81-019)
7. Cloude, S. R. (2010). Polarisation: Applications in Remote Sensing. Oxford University Press. (DOI: 10.1063/1.3502550)
8. Falcon, N.L. (1961). Major earth-flexuring in the Zagros Mountains of south-west Iran. Quarterly Journal of the Geological Society of London, 117(1–4), 367-376. (DOI: 10.1144/gsjgs.117.1.0367)
9. Hessami, K., Koyi, H., & Talbot, C. (2001). The significance of strike-slip faulting in basement Zagros fold and thrust belt. Journal of Petroleum Geology, 24(1), 5-28. (DOI: 10.1111/j.1747-5457.2001.tb00659.x)
10. Lee, J.S., & Pottier, E. (2017). Polarimetric Radar Imaging: From Basics to Applications. CRC Press. (DOI: 10.1201/9781420054989)
11. Moreira, A., Prats-Iraola, P., Younis, M., Krieger, G., Hajnsek, I., & Papathanassiou, K. (2013). A Tutorial on Synthetic Aperture Radar. IEEE Geoscience and Remote Sensing Magazine, 1(1), 6-43. (DOI: 10.1109/MGRS.2013.2248301)
12. Motiei, H. (1993). Stratigraphy of Zagros [in Persian], in: Treatise on the Geology of Iran. Geological Survey of Iran Publications.
13. Sella, G., Dixon, T., & Mao, A. (2002). REVEL: A model for recent plate velocities from space geodesy. Journal of Geophysical Research, 107(B42081), (DOI: 10.1029/2000JB000033)
14. Sherkati, S., & Letouzey, J. (2004). Variation of structural style and basin evolution in the central Zagros (Izeh zone and Dezful Embayment), Iran. Marine and Petroleum Geology, 21(5), 535-554. (DOI: 10.1016/j.marpetgeo.2004.01.007)
15. Sherkati, S., Molinaro, M., Frizon de Lamotte, D., & Letouzey, J. (2005). Detachment folding in the Central and Eastern Zagros fold-belt (Iran): salt mobility, multiple detachments and late basement control. Journal of Structural Geology, 27(9), 1680-1696. (DOI: 10.1016/j.jsg.2005.05.010)
16. Shimada, M., Isoguchi, O., Tadono, T., & Isono, K. (2010). PALSAR radiometric and geometric calibration. IEEE Transactions on Geoscience and Remote Sensing, 47(12), 3915-3932. (DOI: 10.1109/TGRS.2009.2023909)
17. Touzi, R., Bhattacharya, A. (2011). Polarimetric SAR urban classification using the Touzi target scattering decomposition. Canadian Journal of Remote Sensing, 37(4), 323-332. (DOI: 10.5589/m11-042)